Charge storage properties of aqueous halide supercapatteries with activated carbon and graphene nanoplatelets as active electrode materials

Bamidele Akinwolemiwa,[a] Chaohui Wei,[a] Qinghua Yang,[b] George Z. Chen[b,c,*]

[a] *International Doctoral Innovation Centre, Faculty of Science and Engineering, The University of Nottingham Ningbo China, Ningbo 315100, People's Republic of China.*

[b] *Department of Chemical and Environmental Engineering, Faculty of Science and Engineering, The University of Nottingham Ningbo China, Ningbo 315100, People's Republic of China.*

[c] *Department of Chemical and Environmental Engineering, and Advanced Materials Research Group, Faculty of Engineering, The University of Nottingham, Nottingham NG7 2RD, United Kingdom.*

* E-mail: george.chen@nottingham.ac.uk

Abstract: Device level performance of aqueous halide supercapatteries fabricated with equal electrode mass of activated carbon or graphene nanoplatelets has been characterised. It was revealed that the surface oxygen groups in the graphitic structures of the nanoplatelets contributed towards a more enhanced charge storage capacity in bromide containing redox electrolytes. Moreover, the rate performance of the devices could be linked to the effect of the pore size of the carbons on the dynamics of the inactive alkali metal counter ion of the redox halide salt. Additionally, the capacitive response of aqueous halide supercapatteries with graphene nanoplatelets as the electrode material may be attributed to the combined effect of the porous structure on the dynamics of the non-active cations, and a possible interaction of the $Br^-/(Br_2 + Br_3^-)$ redox triple with the surface oxygen groups within the graphitic layer of the nanoplatelets. Generally, it has been shown that the surface groups and microstructure of electrode materials must be critically correlated with the redox electrolytes in the ongoing efforts to commercialise these devices.

Keywords: *supercapattery, redox electrolyte, carbon materials, energy efficiency, device engineering.*

1. Introduction

In principle, improving the electrode capacitance and operating potential window of the electrode | electrolyte (E|E) interface is a general strategy to obtain high energy supercapacitors and supercapacitor-battery hybrids, i.e. supercapatteries. This has been demonstrated by adopting electrodes with high capacitance or capacity[1], high voltage electrolyte[2], coupling the former with the latter[3], or through device design strategies such as un-equalisation of electrode capacitances[4], or the use of bi-electrolyte cells[5, 6]. In recent years, the use of electrolytes that display redox activity within the stability range of the E|E interface has gained prominence[7]. This is due to the simplicity of the method, and the possibility of designing cells with fairly high energy capacities[8, 9].

In addition to the selection and characterisation of a wide range of dissolved redox species[10] (DRS), attempts have been made to improve the performance metrics through materials modification. For example, self-discharge has been reduced through reversible solid-state complexation of the products (Br_2/Br_3^-) from the oxidation of bromide ion (Br^-) as DRS[11], or through the electrorheological effects of liquid crystals[12]. Also, the use of an electrode material that provides a high overpotential for the redox reaction of the Ce^{4+}/Ce^{3+} in aqueous (acidic) media has been shown to be greatly dependent on the surface property of the graphene-felt active electrode material used[13]. Likewise, the efficiency of charge storage when $VOSO_4$[14] or $CuCl_2$[15] was used as the redox electrolyte has been linked to the interaction of the VO^{2+} or Cu^{2+} cations respectively, with surface oxygen groups.

Summarily, the porosity of the carbons together with the surface physicochemical properties are two main features that have been used to assist understanding and develop supercapacitors comprising of DRS. Along these lines, it has been described that for inert electrolytes, the porous volume of the electrode acts as a “dead-volume”. This is because, when the dissolved ions are inert, charging simply

entails their withdrawal from the liquid phase, towards the Helmholtz layer. Conversely, with redox electrolytes, this "dead volume", if provided by pores of sizes that can entrap the electro-generated ions, can act as a "functional-volume"[16].

In a previous work, we reported the role of the thermodynamic properties of halides and their effects on the charging of an activated carbon electrode in supercapatteries. Therein, we demonstrated that the electrode potential of the $Br^-/(Br_2 + Br_3^-)$ redox triple resulted in improved device charge capacity through a combined double layer and Nernstian storage mechanism[9]. In the current report, we describe the device-level performance of supercapatteries fabricated from two different commercial carbon electrodes with bromides as DRS. This was done by correlating the porous and surface physicochemical characteristics of these electrodes with the properties of the redox electrolytes such as the concentration and hydrous sizes of the active bromide and dissolved cations, respectively.

2. Experimental

An activated carbon (AC-2) powder (i.e. HEC-8A obtained from Fuzhou Yihuan Carbon Co. China), and GNP (i.e. graphene nanoplatelets Grade C750 obtained from XG Sciences USA) were active materials of the electrodes used in this work. For electrode preparation, the carbon material was mixed with polytetrafluoroethylene (PTFE, 60% wt in water, Sigma-Aldrich UK) in a weight ratio of 95:5, with ethanol as the dispersing medium. The slurry obtained from this mixture was stirred at 50 ^oC to evaporate ethanol, and the produced paste was roll-pressed (on a DG 200L Roll Press, MAX China) into a blanket which was dried at 120 ^oC for 12 hours. The dried blanket was cut, weighed (Sartorius microbalance, ± 0.01 mg), and die pressed under a force of 2 tonnes into cylindrical pellets (diameter: 13 mm). The pressed pellets were further dried at 80 ^oC in air for at least 10 hours.

The electrode mass in the prototype cells was 15.00 ± 0.01 mg, and the pressed pellets used in cell

fabrication had an areal mass loading of at least 11.30 mg/cm^2 with thickness of ca. 240 μm.

A T-shaped Swagelok cell with titanium current collectors was used in assembling the 2-electrode cell. In order to ensure that equal volumes of electrolytes were used in all the fabricated cells, the mass of the soaked electrodes and separator were first measured, and then a specific volume of electrolyte was added to the cell[7, 8]. The separator membrane Glassy paper (GF/D, Whatman) was soaked in the electrolyte before use. For the 3-electrode tests, a standard calomel reference electrode (CHI 150 SCE from CH Instruments) was inserted into the T-shaped Swagelok cell, comprising of working and counter electrodes of masses equal to ca. 5.00 mg and 30.00 mg respectively.

All electrolytes were bubbled by Ar (99.8%) for at least 20 min. before their use for soaking the electrodes or separators under vacuum for an hour, followed by further Ar bubbling for another 10 min. All chemicals used in this work i.e. KCl, LiBr, NaBr, KBr, $MgBr_2$, Na_2SO_4, $MgSO_4$ (all with purity > 99% and obtained from China Sinopharm) were used as received.

Electrochemical characterisations were carried out on the Princeton Multichannel Workstation equipped with the PMC-1000 and PMC-2000 modules, and the VersaStudio software package. Equations 1 and 2 were used to calculate the charge efficiency and capacitance.

Charge efficiency (η_Q): $$\eta_Q = \frac{Q_d}{Q_c} \times 100\% \quad (1)$$

Capacitance (C): $$C = \frac{Q_+ + Q_-}{2\Delta E} \quad (2)$$

where Q_d and Q_c are the passing charges when recording the Galvanostatic charging and discharging plot (GCD), Q_+ and Q_- are those during the positive and negative potential scans for recording a cyclic voltammogram (CV), respectively, and ΔE is the maximum potential range for recording a rectangular CV, i.e. the capacitive potential range (CPR). The following equations were used to calculate the

performance of cells obtained from the GCDs.

Specific energy (W_{sp}): $$W_{sp} = \int_{U_{min}}^{U_{max}} IdU = I \int_{t=0}^{t=t} U_d(t)dt \quad (3a)$$

Energy efficiency (η_W): $$\eta_W = \frac{\int U_d(t)dt}{\int U_c(t)dt} \times 100\% \quad (3b)$$

Where $U_d(t)$ and $U_c(t)$ are the cell voltage as a function of the time, t, of discharging and charging, respectively, in the GCD measurement of the cell, and I is the mass normalised current (or specific current or current load) against the total mass of active materials on both the positive electrode (positrode) and negative electrode (negatrode) (i.e. $m_+ + m_-$) in the cell with the unit in A/g (or mA/g). The positrode and negatrode of all the cells reported in this work are equal.

Electrochemical impedance spectroscopy was carried out with the aid of the Princeton Multichannel Workstation (PMC-2000 module). To carry out the impedance measurement at a given applied (or cut-off) voltage (U_L), the voltage of the cell was scanned at 5 mV/s from open circuit voltage to U_L after which a sinusoidal voltage of 10 mV was applied to carry out the EIS measurements. The frequency range was from 100 kHz to 0.01 Hz.

The equivalent circuit displayed in the inset of Fig. 11(b1) was used to simulate the circuit parameters. In Fig. 11(b1) R_1 and R_2 corresponds to series and charge transfer resistances respectively. Whilst CPE_1 and CPE_2 are constant phase elements which correspond to frequency dependent impedance relating to capacitive storage, and semi-infinite linear diffusion of reacting species, respectively[17, 18]. For the graphical interpretation of the Nyquist plots, the frequency dependent capacitance $C(\omega)$ defined by Eq. 4 was used.

$$C(\omega) = C'(\omega) - j\, C''(\omega) \quad (4)$$

Where

$$C'(\omega) = \frac{-Z''(\omega)}{\omega\left|Z(\omega)\right|^2} \quad (5a)$$

and

$$C''(\omega) = \frac{-Z'(\omega)}{\omega\left|Z(\omega)\right|^2} \quad (5b)$$

Herein, $C'(\omega)$ and $C''(\omega)$ are the real and imaginary parts of the capacitance $C(\omega)$, respectively. In general, the value of $C'(\omega)$ at low frequency (which in this experiment corresponds to f = 0.01 Hz) can be considered as the capacitance of the cell. On the other hand, $C''(\omega)$ corresponds to the dissipation of energy which may be due to irreversible processes[19].

For example, at the high frequency region, the non-frequency dependent ohmic resistance (R_1 from the inset in Fig. 11 (b1)), is dominant, i.e. the characteristic of the device is resistive. At the medium frequency region, the charge transfer resistance of the cell which is a kinetic parameter of the device can be observed. It is then followed by the diffusion region which can be used to explain the diffusion of the species within the porous carbon electrode [20].

The dispersed capacitance region thus corresponds to the interfacial charge within the porous matrix of the carbon, and broadly reflects the complex contribution of the porous structure of the carbon to the capacitance. In reference to the Nyquist plot, the extent of deviation of the dispersed frequency region from ideality (90^o) can also be used to describe the porous property of the electrode, and it also reflects the dissipative features displayed by the device [19, 21]. Thus, considering the expressions given in Eq. 5 (a and b), relative to the Nyquist plot, when

$$\frac{C'(\omega)}{\lim_{\omega\to 0} C'(\omega)} = 0 \quad (6a)$$

the system is mainly resistive. Moreover, when

$$\frac{C'(\omega)}{\lim_{\omega \to 0} C'(\omega)} = 1 \qquad (6b)$$

capacitive properties would predominate.

In practice, the mathematical limit described in Eq. 6 refers to the lowest frequency of the applied AC signal (0.01 Hz in this experiment). Accordingly, the imaginary component of the capacitance i.e. $C''(\omega)$ would attain a maximum value at a specific frequency f_0 which can be correlated with a given 'time constant', $\tau = 1/f_0$.

Nitrogen physisorption analysis (at 77 K) was carried out with the aid of the ASAP Micrometrics 2020 Physisorption Analyser. Scanning electron microscope (SEM) from ZEISS was used to obtain the SEM micrographs, whilst images from transmission electron microscopy (TEM) were obtained using the FEI Tecnai F20. X-ray photoelectron spectroscopy (XPS) was carried out using the ESCALAB 250 system. Thermogravimetric analysis (TGA) was conducted using the TG/DTA6300 from SII Nano Technology Inc. in which samples were loaded in the manufacture provided small alumina crucible under air flowing at 300 mL/min. The temperature ramp rate was 10 °C/min. The elemental analysis was conducted on the vario EL cube CHN/S/O element analyser from Elementar.

3. Results and Discussions

3.1. Properties of the activated carbon and graphene nanoplatelets

Figure 1 shows the BET adsorption isotherms and pore size distribution for the two carbons. Fig. 1(a1) indicates AC-2 to be microporous as can be seen from its isotherms which are characterised by a high volume of adsorption at relatively low pressures [22]. The isotherm of GNP (see Fig. 1(b1)) displayed an increase in adsorption at high values of p/p^o, which is indicative of a predominantly mesoporous

material [22-24]. For AC-2, mesopores contributed to ca. 35.81% of the total pore volume, and it had an average pore width of 2.23 nm (with BET-SSA of 1570.51 m^2/g). The pore volume of GNP comprised of ca. 18.54% of micropores, 81.46% of mesopores, and it had an average pore width of 6.22 nm (with BET-SSA of 698.53 m^2/g). This difference in the pore size distribution as can be observed in Fig. 1 (a2 and b2) respectively for AC-2 and GNP, could be used to approximately understand the electrical response of the EDL properties of these carbons, especially with respect to the complementary roles between the mesopores and micropores.

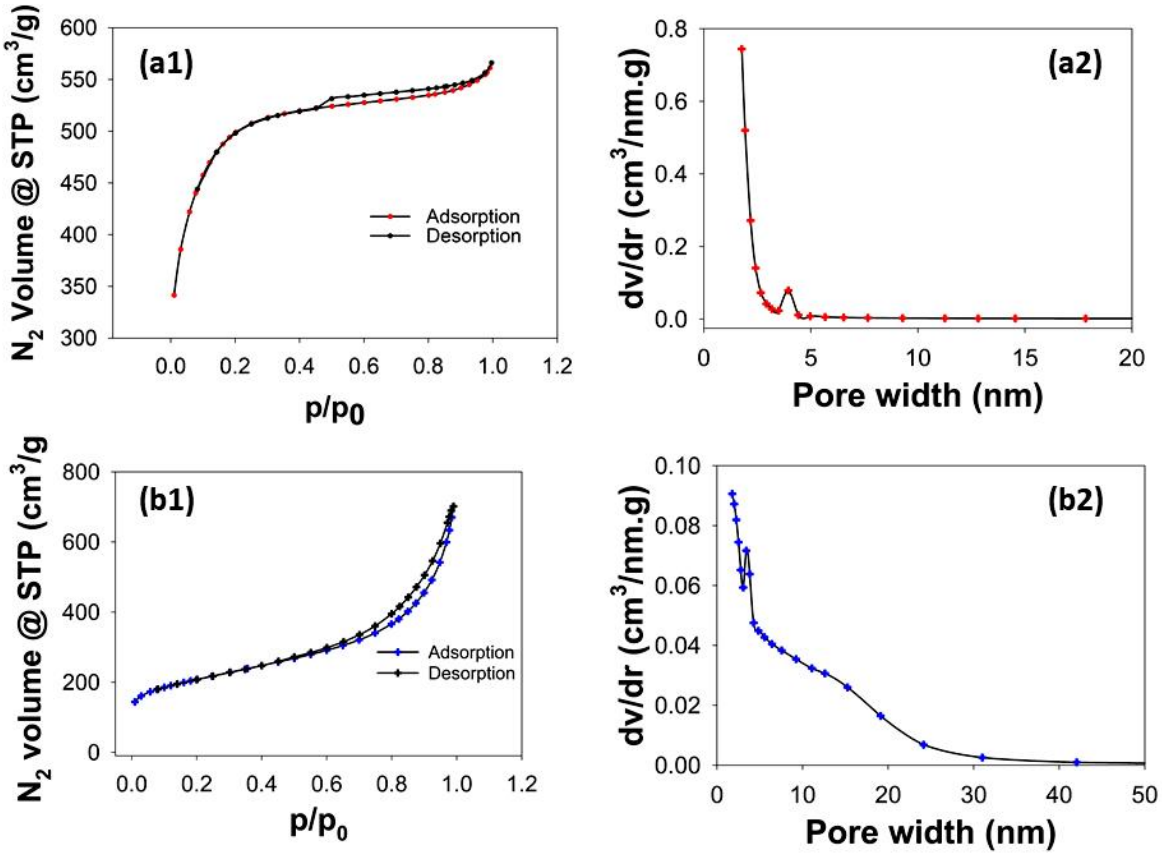

Figure 1: N_2 Physisorption graphs showing the adsorption/desorption isotherms and pore size distribution calculated by the DFT method for AC-2 (a1 and a2), and GNP (b1 and b2).

Table 1: Elemental compositions determined by CHN/S/O elemental analysis

Carbon	C (%)	O (%)	H (%)	N (%)
AC-2	79.60	18.51	1.52	0.28
GNP	82.75	15.27	1.30	0.65

From the elemental analysis of the two carbons as summarised in Table 1, it was observed that AC-2 and GNP comprised of a significant number of surface oxygen groups (SOGs). Accordingly, from the analysis of the X-ray photoelectron spectrographs (XPS) shown in Fig. 2, it was observed that the C/O ratio for AC-2 was slightly lower than that of GNP, in line with Table 1. Moreover, in AC-2, O-C=O was 56.28% whilst C-O accounted for 43.72%. On the other hand, O-C=O and C-O were 62.40% and 37.6%, respectively, in GNP. Generally, these surface properties as revealed by XPS are consistent with the thermal stability of these carbons as observed from the thermo-gravimetric analysis shown in Fig. 3, which shows that some of the surface (quinone or ether) groups in AC-2 and GNP are similar.

Figure 4a shows the SEM image of GNP, which appears as a porous agglomerate. Moreover, the resolution of the structure with TEM revealed the platelet-like microstructure of the crumpled and stacked graphene sheets as shown in Fig. 4 (b1 and b2). The amorphous microstructure of AC-2 is shown by the SEM image of Fig. 4c, which is in line with the general features of activated carbons.

Summarily, these two types of carbons with different microstructures i.e. activated carbon (AC-2) and graphene nanoplatelets (GNP) are typical examples of carbon electrode materials with surface oxygen groups (SOGs). In line with this, the interaction of DRS with GNP which was of particular interest in this study should be analysed. Moreover, because AC-2 represents the typical EDL electrode due to its micoroporous properties, comparisons are always made between the properties of these two materials in order to gain further insight into the mechanisms of interaction of DRS with different carbons.

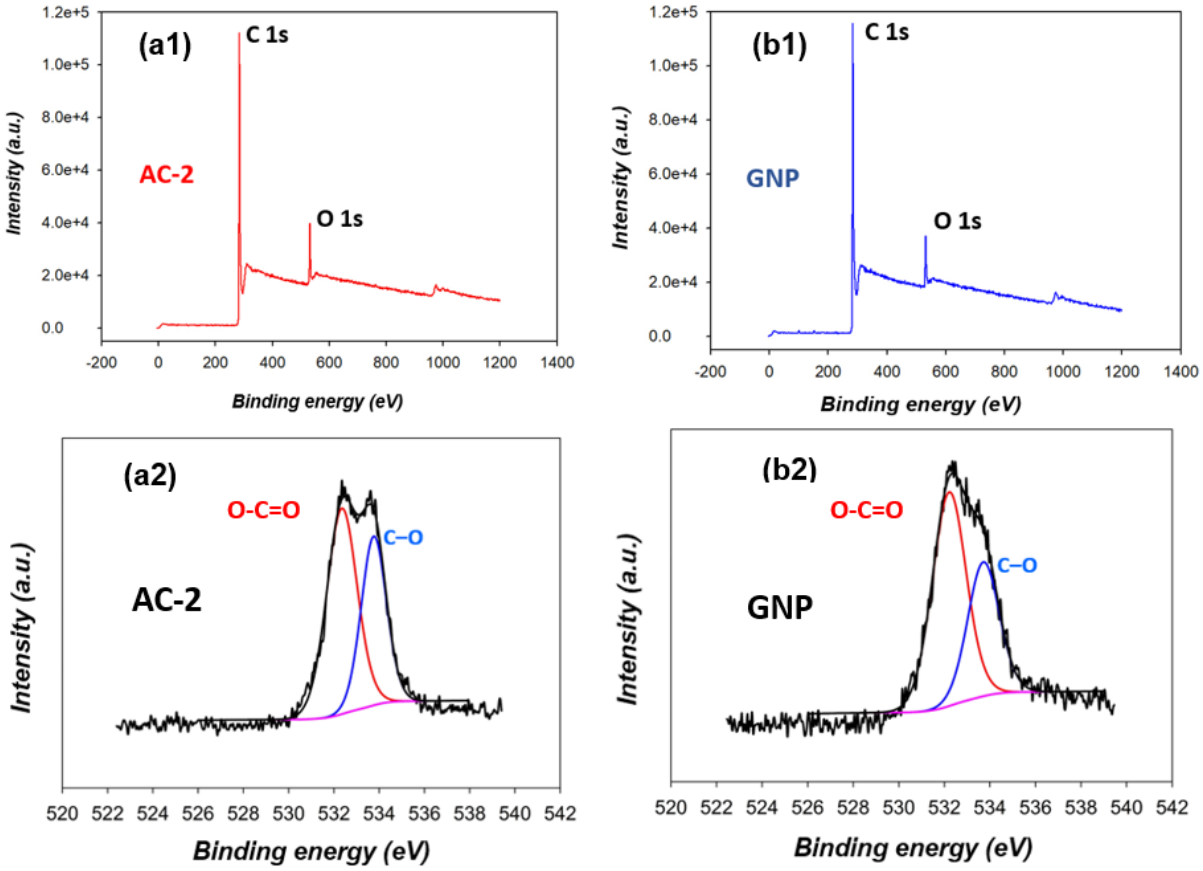

1

2 Figure 2: X-ray photoelectron spectra for (a1) AC-2 (b1) GNP; De-convoluted XP spectra for the O 1s

3 core for (a2) AC-2 (b2) GNP.

4

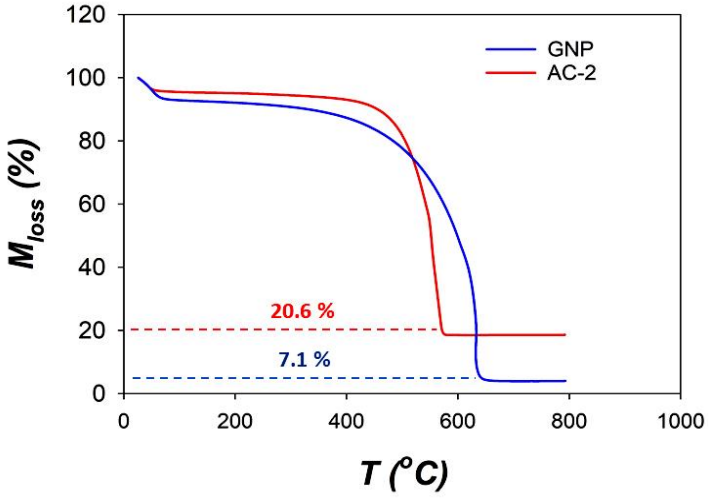

5

6 Figure 3: TGA profiles of AC-2 and GNP in N_2 at 10 °C/min. M_{loss}: loss in mass.

7

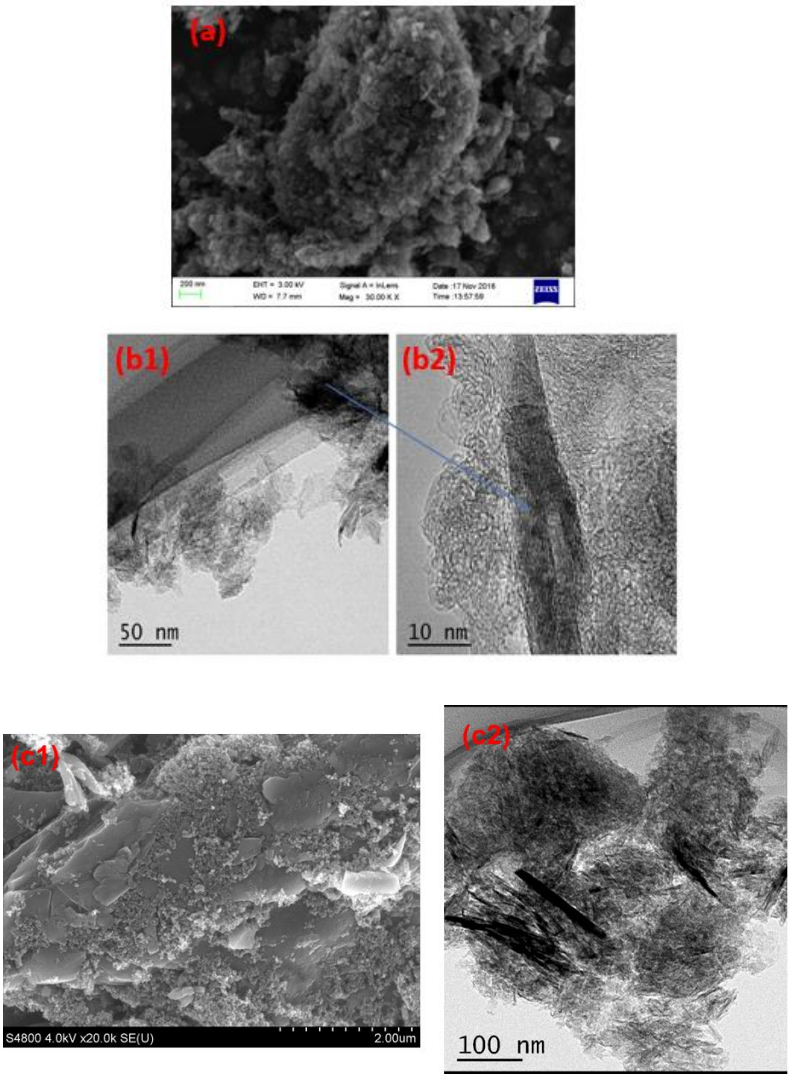

Figure 4: SEM (a) and TEM (b1) images of GNP and increased resolution of b1 (b2), and SEM (c1) and TEM (c2) images of AC-2.

3.2. Comparing EDL capacitors to supercapatteries fabricated with activated carbon and graphene nanoplatelets

The CVs for the cells of equal electrode mass (EEM) comprising of 2.0 mol/L KCl with either AC-2 (2M-KCl-AC-2) or GNP (2M-KCl-GNP) as electrodes are compared in Fig. 5a. The cell capacitance for 2M-KCl-AC-2 was calculated to be 17.1 F/g, and this is slightly larger than 15.2 F/g for 2M-KCl-

GNP. This slight difference in the cell capacitance may be attributed to the higher surface area of the AC-2 electrode. Moreover, an important finding was that when the cells using 2.0 mol/L KBr was considered (see Fig. 5b), the difference in charge capacity between GNP and AC-2 was markedly significant, with the capacity of the former being over 50% larger than the latter. More importantly, this charge capacity enhancement was predominant in the Nernstian feature on the GNP. As shown in Fig. 6, the reaction of the redox triple of $Br^-/(Br_2 + Br_3^-)$ occurring at the positrode is responsible for the enhanced charge capacity observed in Fig. 5b. Descriptions of this combined Nernstian and EDL charge storage mechanism for halide supercapatteries has been provided in detail elsewhere[9].

This observation (cf. Fig 5a and 5b) shows that despite the larger BET-SSA of AC-2 compared to GNP, with the use of redox electrolytes, the pore size distribution particularly the presence of mesopores and possibly the role of the surface reactivity become significant. Surface reactivity corresponds to interactions of solution components with surface groups (e.g. surface oxygen groups) of the carbon[25, 26].

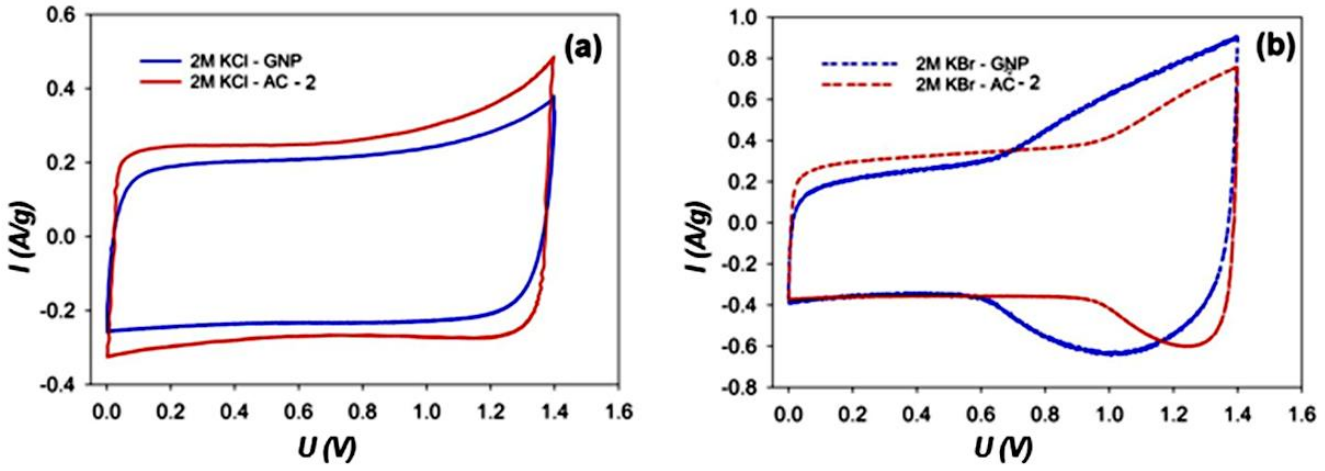

Figure 5: CVs of EEM cells with GNP and AC-2 electrodes using inert 2.0 mol/L KCl (a) and active 2.0 mol/L KBr (b), respectively. Scan rate: 5 mV/s.

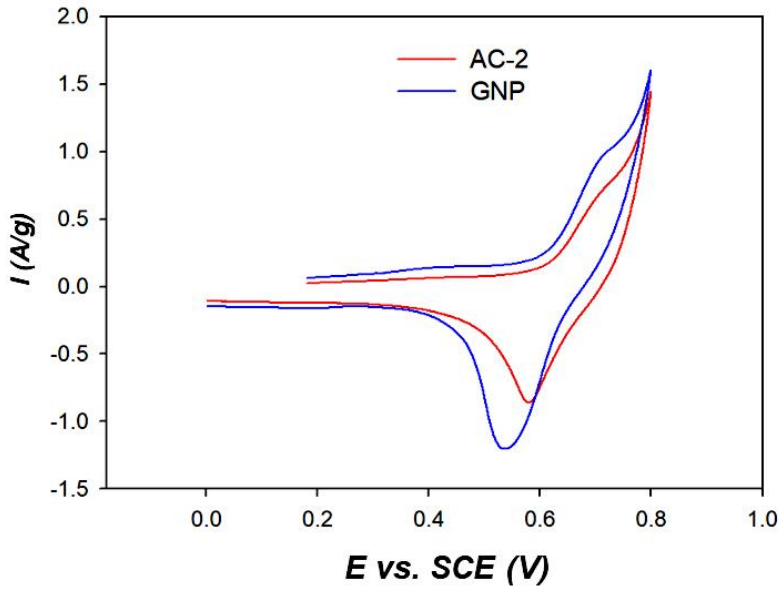

Figure 6: CVs recorded in a three-electrode cell showing charge transfer reactions of the redox triple, $Br^-/(Br_2 + Br_3^-)$ on GNP and AC-2 electrodes in 2.0 mol/L KBr. Scan rate: 5 mV/s.

In addition to the role of the pore size which aids additional entrapment (active volume), this high charge capacity of the GNP using DRS could be attributed to the effective electrosorption of anionic species, Br^- and Br_3^-, within the interlayer of the graphene nanoplatelets. Furthermore, the role of the surface active sites promoting additional surface redox reactions in the GNP may also be significant [27-29]. Such improved electrosorption due to the morphology of the surface might not be observed for the AC-2 which is an amorphous carbon [30, 31]. Thus, the charge storage mechanism of AC-2 in the bromide electrolyte could be attributed mainly to the adsorption and/or entrapment of the products of the redox reaction, with very little contribution from its surface properties.

3.3. Charge storage properties of supercapatteries with AC-2 or GNP as electrodes, and varying concentration of LiBr as electrolyte

Figures 7 and 8 show the CVs and GCD plots at different values of U_L for EEM cells with either AC-2 or GNP as electrodes in electrolytes of different concentrations of LiBr. These CVs and GCD plots were shown at U_L (upper limits of cell voltage) values from 1.6 to 2.0 V, because for practical reasons, this is the voltage range of interest when the effects of the DRS on the devices are to be appraised[9].

From CVs in Fig. 7, it can be noticed that at different values of U_L, the profiles of the cells with similar electrodes were similar, but cells with different electrodes display significantly different charge storage features. Table 2 presents the performance metrics for the cells calculated from the GCD data. These performance metrics are W_c: specific energy for charging, W_d: specific discharge energy (same as W_{sp} i.e. specific energy of the device), W_{eff}: energy efficiency (= W_d/W_c), and Q_{eff}: charge efficiency (=Q_d/Q_c). The cell performance metrics presented in Table 2 were calculated from the GCD plots of the cells in Fig. 8, i.e. at a current load of ± 0.5 A/g (ca. ± 15.0 mA of applied current).

Generally, at all voltages and concentrations, the discharge or specific energy (W_d) of GNP cells were greater than those displayed by AC-2 cells. The performance metrics of W_{eff} and Q_{eff} are linked to the charge and mass transfer of the DRS at the E|E interface, thermodynamics and reversibility of the redox reactions, and the electro-sorption/desorption of both active and non-active species inside the porous matrix [8, 11, 32, 33].

These properties are in turn influenced by the porosity and the physicochemical properties of the surface. For example, the generally high Q_{eff} values observed for the cells, particularly at U_L = 1.6 V,

can be attributed to the highly reversible reaction of the Br^- / (Br_2 + Br_3^-) redox triple at the carbon | electrolyte interface on the positrode, see Fig. 6. The variation in W_{eff} is an important property that can

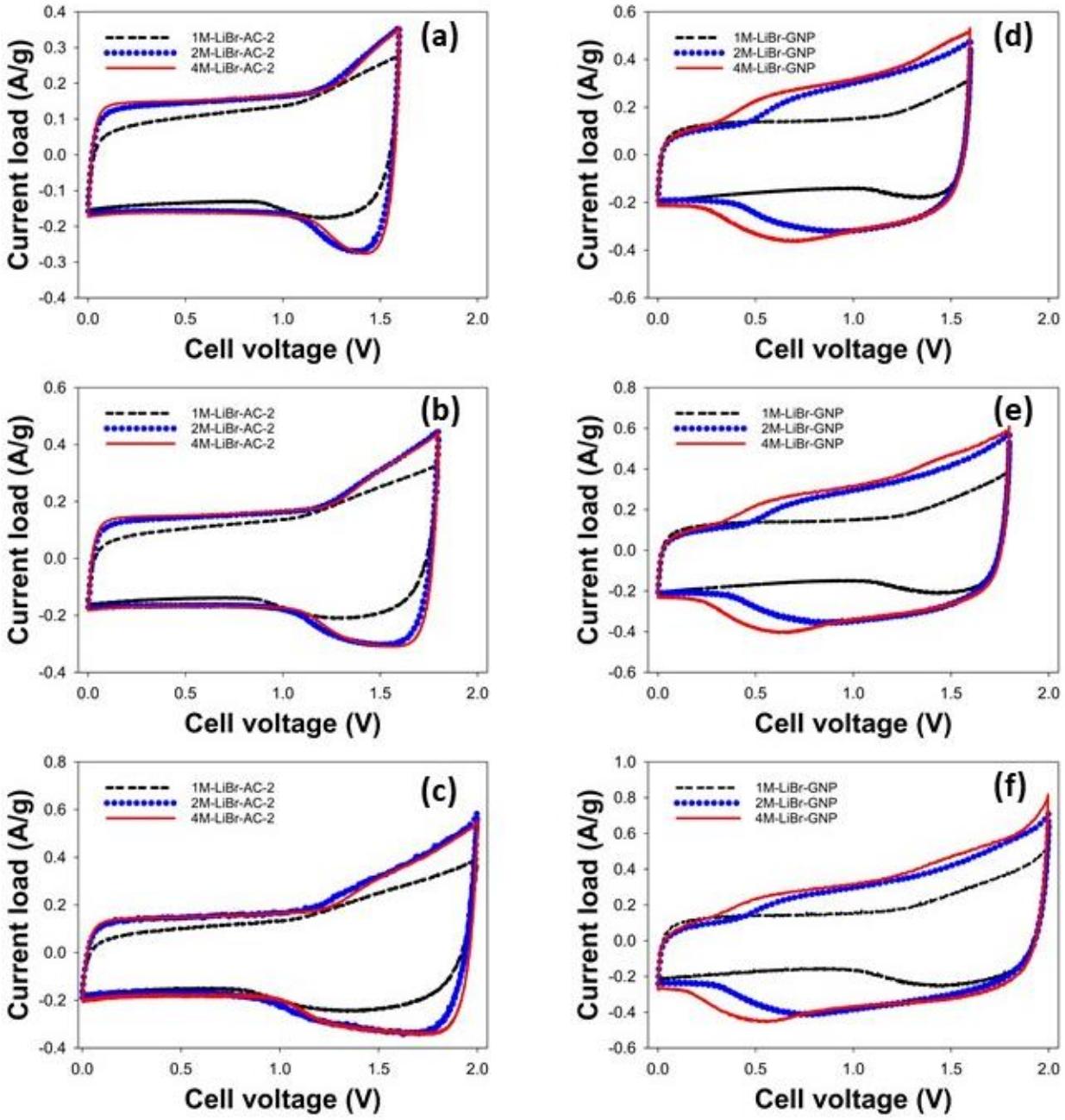

Figure 7: CVs at different upper voltage limits for EEM cells with electrolytes of varying concentration of LiBr assembled with: AC-2, U_L = 1.6 V (a), 1.8 V (b) 2.0 V (c) and GNP, U_L = 1.6 V (d), 1.8 V (e) 2.0 V (f). Scan rate: 10.0 mV/s.

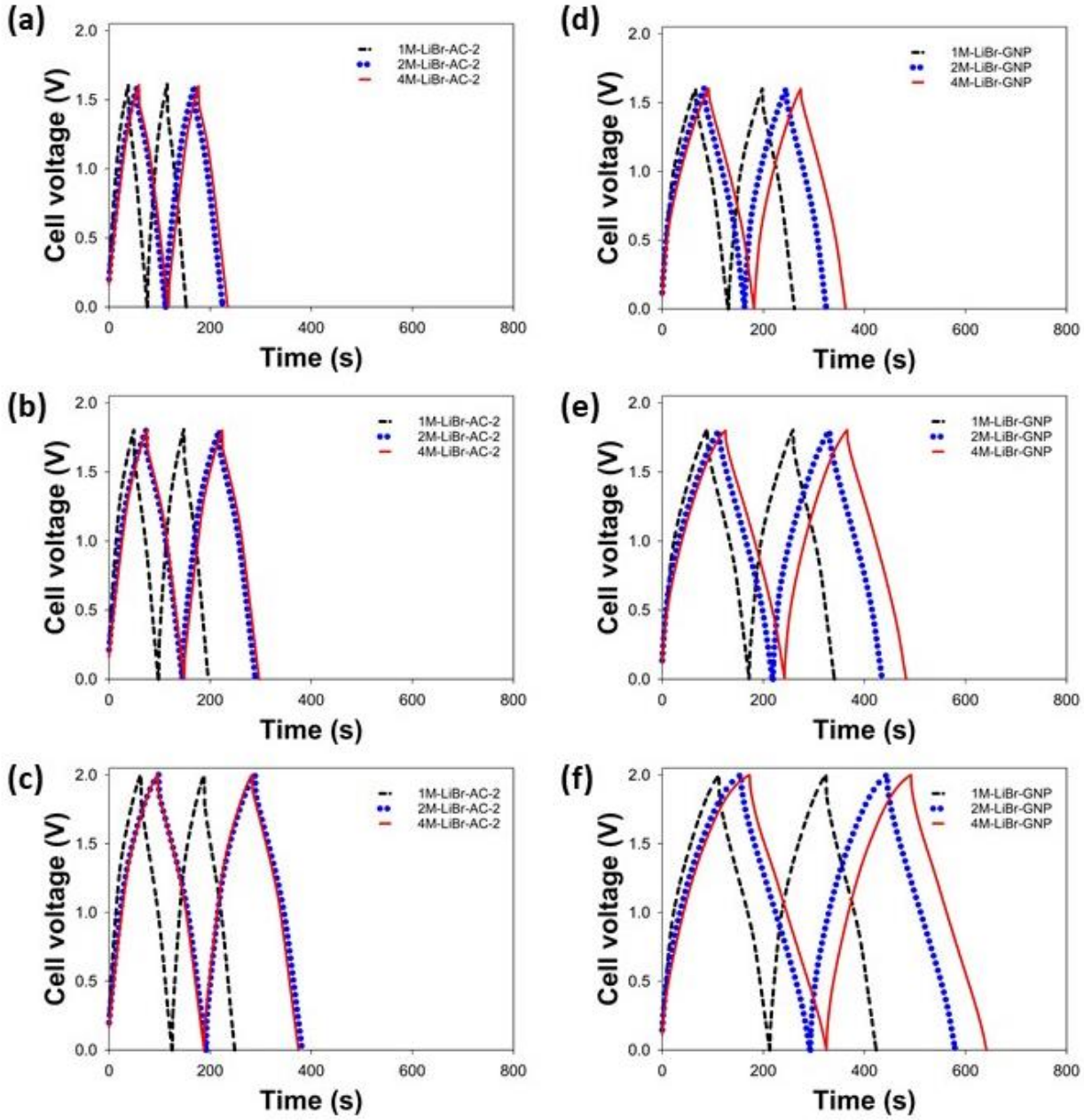

Fig. 8: GCD plots at different upper voltage limits for EEM cells with electrolytes of varying concentration of LiBr assembled with: AC-2 at U_L = (a) 1.6 V (b) 1.8 V (c) 2.0 V and GNP at U_L = (d) 1.6 V (e) 1.8 V and (f) 2.0 V. Current load: $\pm$ 0.5 A/g (ca. $\pm$ 15 mA of applied current).

Table 2: Performance metrics at different cell voltage limits (U_L) of EEM supercapatteries with (a) AC-2 and (b) GNP as electrodes in electrolytes of different LiBr concentrations.

(a)

Cell	U_L (V)	W_c (Wh/kg)	W_d (Wh/kg)	W_{eff} (%)	Q_{eff} (%)
1M-LiBr-AC-2	1.6 V	11.6	7.7	66.4	95
	1.8 V	17	11.6	68.2	94.1
	2.0 V	24.2	16.4	67.8	95.3
2M-LiBr-AC-2	1.6 V	16.3	12.5	76.7	96.6
	1.8 V	24.3	18.3	75.3	97.3
	2.0 V	37.2	27.8	74.7	94.9
4M-LiBr-AC-2	1.6 V	16.2	13	80.2	96.7
	1.8 V	24.5	19.2	78.4	96.1
	2.0 V	35.4	27.5	77.7	95.8

(b)

Cells	U_L (V)	W_c (Wh/kg)	W_d (Wh/kg)	W_{eff} (%)	Q_{eff} (%)
1M-LiBr-GNP	1.6 V	19.8	14.7	74.2	95.5
	1.8 V	29.63	21.3	71.9	93.2
	2.0 V	42.6	27.9	65.5	90
2M-LiBr-GNP	1.6 V	24.6	19	77.2	96.4
	1.8 V	37.9	28.9	76.3	92
	2.0 V	58.3	36.1	61.9	88.2
4M-LiBr-GNP	1.6 V	26.8	21.3	79.5	95.7
	1.8 V	41.4	30.2	72.9	93.6
	2.0 V	63.3	39.1	61.8	89.3

be used to explain the extent of utilisation of the redox species, together with the role of the porous characteristics, the physicochemical properties of the surface, and possibly morphology of the carbons.

Although, it is difficult to ascertain which property predominates in the displayed charge storage performance of the GNP electrode, the larger pores of GNP, might reduce the effects of steric

hindrance, and can also accommodate additional product of the redox reaction, even at higher concentration of the ions [1, 27]. On the other hand, the smaller pores of AC-2 may increase confinement of ions which could result in a high degree of steric hindrance [34]. Hence, even with increased generation of ions from the redox action they may not contribute to increasing storage within the porous matrix of AC-2 [35].

Also, the sensitivity of the Q_{eff} and W_{eff} of the GNP electrode to concentration might further support the claim that in addition to the role of the mesopores being capable of holding more charge, there might be the presence of additional reaction of the redox triple of Br^- / (Br_2 + Br_3^-) with the GNP surface. Such observations were described as due to possible electro-catalytic effects of the graphitic interlayer/lattice on the activity of some redox ions [27, 29, 36]. This is in contrast to that of AC-2 whose charge storage is predominantly due to the adsorption or entrapment of the generated species, with strong van der Waals interactions being responsible for any additional or enhanced adsorption [31, 37].

Furthermore, the actual mechanism of ion adsorption (or entrapment) for different cation-anion combination is quite specific to the types of ions involved, and could also be determined by the nature of the solvation shells around or between the ions, i.e. type of contact between the ions [32]. For example, the individual hydration shells of ions could be in contact, ions could share the hydration shells, or ions could be in direct contact with one another covered by the hydration shell[32]. In line with this, different ion-contact types could result in significantly different ion-electro-sorption/charge compensation mechanisms within the porous matrix of the carbon. For instance sorption of LiBr in mesoporous carbon has been linked to the geometric properties of the pores [38]. Accordingly, the entirety of the solvated co-ions may have to enter into the pores to contribute to charge storage.

With this line of thought, any mechanism of storage that involves hydrated Li^+ ions, be it desorption/adsorption, or ion-exchange, would be kinetically difficult in AC-2, compared to GNP. Thus, the increase in charge and energy efficiency of AC-2 with an increase in concentration from 1.0 to 2.0 mol/L LiBr could imply that a combined diffusion and migration of the electro-generated species into the pores is necessary for AC-2 to effectively store charge. Thus, at a high enough concentration such diffusion mechanisms become less important for charge storage in AC-2. Hence, a concentration increase from 2.0 to 4.0 mol/L LiBr did not increase significantly the charge capacity for AC-2.

Contrastingly, for GNP, the concentration of LiBr resulted to an increase in the measured W_d at all values of U_L. This increase in capacity with concentration can thus be closely linked to an additional surface reactivity of the GNP which may be aided by the improved electro-sorption provided by the morphology of the graphene layers.

The presence of low voltage current bumps on the CVs of GNP at high concentration (2.0 or 4.0 mol/L) when U_L = 1.8 or 2.0 V, could be attributed to the combination of the strong polarisation potential of the Li^+ ion and the existence of a higher diffusion gradient during the charge/discharge of the mesoporous carbon (this aspect will be re-visited in section 3.4 where the features of the cells with different cations are presented). Moreover, this diffusion is confined within the mesoporous carbon, and as such it does not shuttle to the negatrode. In line with this, the migration effects due to localised mass transport of the species within mesopores seem to be significant when LiBr was used with the mesoporous GNP.

To further ascertain the role of the surface activity of the carbons on the observed charge storage features, two different cells with GNP or AC-2 electrodes were each cycled at a current load of 0.5 A/g and cut-off voltage of 2.0 V. As shown in Fig. 9, although both cells displayed marked degradation reaching the so-called “end of life criterion” (EoLC) within the cycling duration, still, the degradation

of GNP was more pronounced than that of AC-2. Note that the EoLC has been suggested as a measure of the ultimate stability of supercapacitors, and the cut-off point is 80% of the initial discharge energy/capacity [39]. The degradation in the energy capacity of the cells with cycling can be linked to the irreversibility in the redox reactions which might include decomposition reactions [40, 41].

Furthermore, the quicker degradation of GNP compared to AC-2 may be linked to the role of defects and surface active sites of this electrode under cycling. This could also be evidence of its high surface reactivity i.e. the additional interaction between the Br^-/ (Br^-_3 + Br_2) species and the surface of the GNP due to enhanced electro-sorption. This additional interaction could thus result in the expansion of the interlayer spacing of the graphitic structure of the GNP, since the charge storage mechanism of GNP may also involve the de-/insertion of Br^-/ Br^-_3 [28, 31].

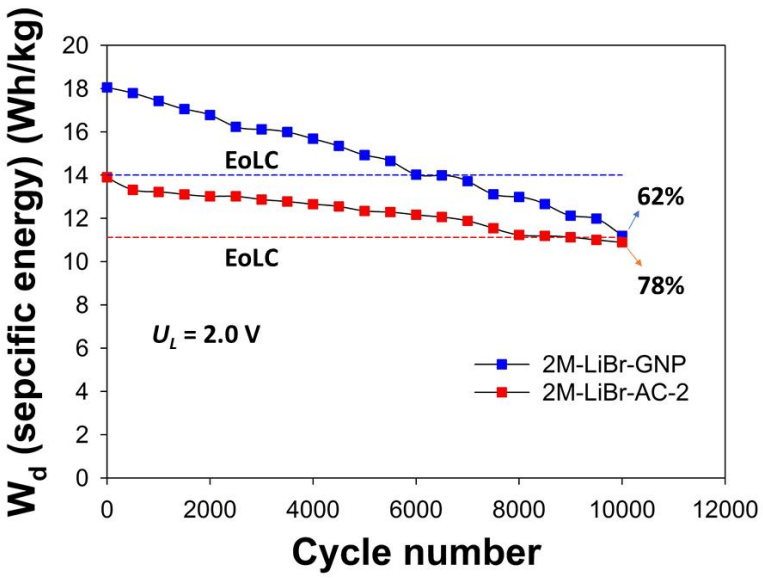

Figure 9: Cycling stability of EEM cells with 2.0 mol/L LiBr and AC-2 or GNP electrodes. Current load = 0.5 A/g (±15 mA of applied current) at upper cell voltage limits U_L of 2.0 V. EoLC: "End of Life Criterion", i.e. 80% of the initial discharge energy.

3.4. Correlating electrode properties with non-active cations of the dissolved redox species

The properties of EEM cells with 2.0 mol/L LiBr, NaBr, or KBr with either AC-2 or GNP as electrodes, were analysed. As presented in Fig. 10(a1) the U_{redox} for the GNP cell with LiBr is much lower than that for either NaBr or KBr, see Fig. 10(b1 and c1). Note that U_{redox} has been described as the cell voltage where the contribution of the DRS to the charge storage of the cell sets in [9]. This observation points out to the role of the polarisation power of the Li^+ in determining the diffusion of the bromide ion during charging/discharging of the cell with GNP.

In Fig. 10 (a2, b2, and c2) it can be seen that aside from the charge capacity increase, at 10.0 mV/s, the features of the cells using AC-2 with all electrolytes were generally identical, with the U_{redox} been comparable. This indicates that the U_{redox} observed for cells is strongly dependent on the polarisation power of the cation together with the nature of the pores. The significance of this is that, when DRS are being selected for highly graphitised (and mesoporous) carbons which may favourably interact with the products of the redox species, attention must also be paid to the counter-ion in terms of not just the hydrated crystal radius (which is the parameter always scrutinised for EDL research and applications), but also with regards to the polarisation power of the cation, which has significant effects on the performance of the device.

With regards to rate performance, it was noticed that at 100.0 mV/s all the cells using GNP generally retained the features of the bromide contribution. That is, apart from the expected decrease in charge capacity at high rates, the features of the bromide ion were still obvious in the cells with GNP electrodes. On the other hand, at 100.0 mV/s, the features of the bromide contribution were generally lost for 2M-LiBr-AC-2, which displayed an almost rectangular CV, whilst 2M-NaBr-AC-2 showed only a slight contribution from the Nernstian properties of the DRS (cf. Fig 10 a2 and b2). On the other hand, a relatively good rate performance was observed for 2M-KBr-AC-2 (Fig. 10 c2), compared to

2M-LiBr-AC-2 and 2M-NaBr-AC-2. The most important property herein is that whilst the highly mesoporous GNP displayed high rate properties i.e. its charge storage profile was retained at high scan rates irrespective of the cations, AC-2 on the other hand displayed a sensitivity to the size of the cations, because only the supercapattery with smaller hydrated K^+ ions were able to retain similar features at higher scan rate (Fig. 10 c2).

The charge storage mechanism in carbon based EDL electrodes is determined by the porosity of the electrode and its effects on the migration of ions under the influence of an electric field. The most general albeit approximate description is that when an electrode material has stratified pores, the mesopores would aid the transport of ions, i.e. serving as conduits whilst the EDL would be formed within the matrix of the micropores [20, 42].

Moreover, when these species are within the pores, other properties such as surface groups, specific adsorption (e.g. electro-sorption on the pore walls), or even the mechanism of charge compensation of the EDL, could also have effects on the redox properties of these DRS. Thus, charging within the pores of nanostructured carbons has been linked to the conjoined action of steric hindrance and the ability of the charged species (active and non-active) to adsorb within the porous matrix of the carbon [34, 43]. In line with this, it is suggested that the porous property of the electrode determines the dynamics of the charge compensation mechanism when the hydrated properties of the dissolved ions are considered.

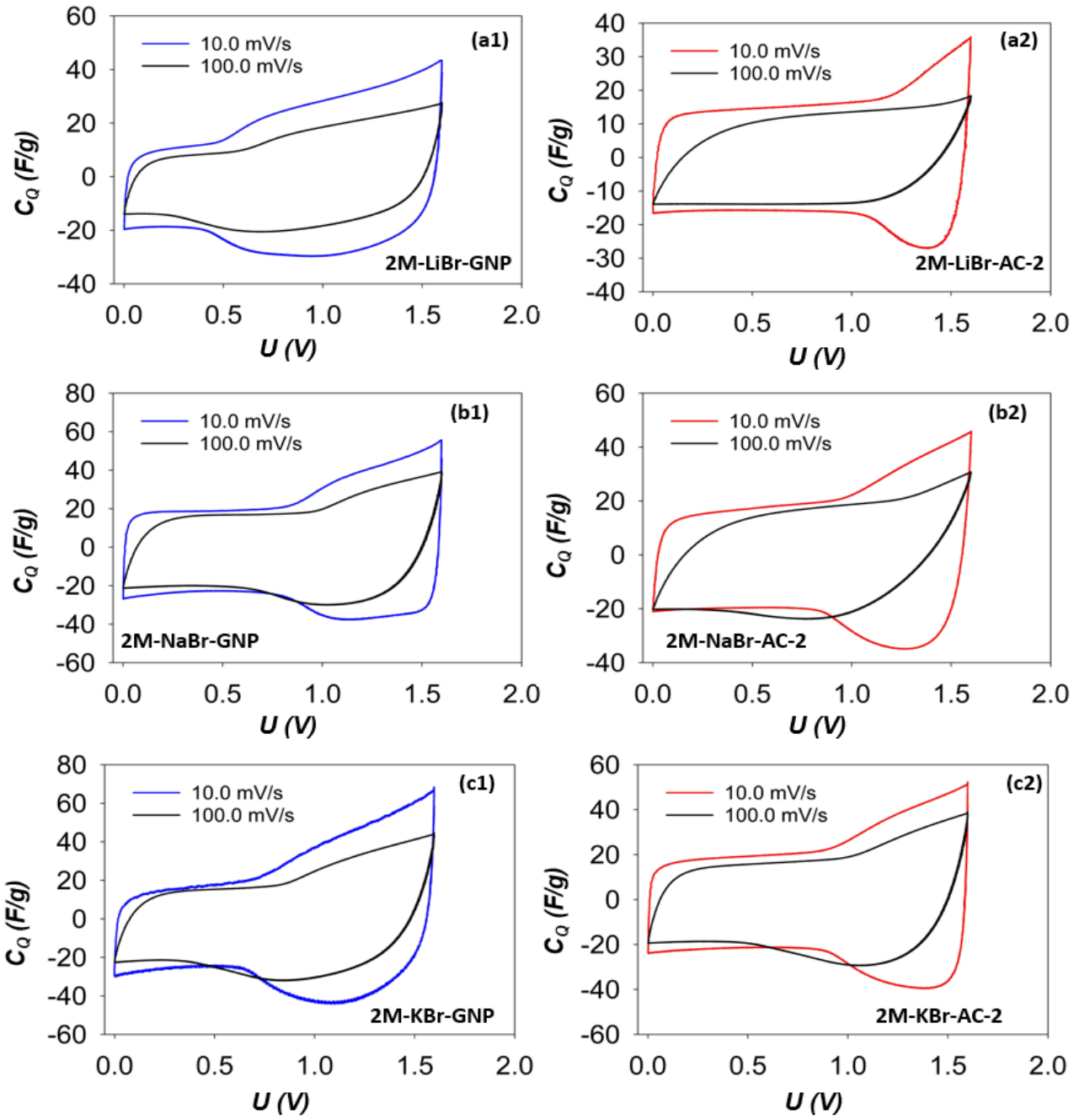

1

2 Figure 10: CVs of different EEM cells showing the cation effects: 2M-LiBr-GNP (a1), 2M-LiBr-AC-2

3 (a2), 2M-NaBr-GNP (b1), 2M-NaBr-AC-2 (b2), 2M-KBr-GNP (c1), and 2M-KBr-AC-2 (c2).

4

3.5. Role of cations in the performance of GNP electrodes with bromides as redox electrolytes or redox additives to inert aqueous electrolytes

Due to the comparatively efficient transport of ions within the porous matrix of the mesoporous GNP, coupled with possible enhanced electro-sorption of the Br^- and Br_3^- ions, the correlation between large hydrated cations and the porous property were further investigated. This was done by comparing the properties of EEM cells with GNP electrodes using either Li or Mg bromides as DRS.

In the cells investigated, the ionic strength of the bromide ion was made to be equal, thus GNP EEM cells with equal volumes of 4.0 mol/L LiBr (called as 4M-LiBr-GNP) and 2.0 mol/L $MgBr_2$ (called as 2M-$MgBr_2$-GNP) were fabricated. It was observed that the charge capacity of 4M-LiBr-GNP was ca. 8.34% less than that of 2M-$MgBr_2$-GNP (see Fig. 11a).

Moreover, the most striking properties of the cells of 4M-LiBr-GNP and 2M-$MgBr_2$-GNP can be observed on the impedance spectra shown in Fig. 11b. Herein, it was noticed that although the R_{CTR} (charge transfer resistance which corresponds to R_2 in the inset of Fig. 11(b1)) of 4M-LiBr-GNP was at least twice of that of 2M-$MgBr_2$-GNP, still their capacitive responses were comparable with a switching (or relaxation) time of ca. 7.94 s (see Fig. 11c). This shows that the R_{CTR} of the GNP electrode was strongly affected by the size of the cations, which could be attributed to the polarisation power of the cation to the Br^- and/or Br_3^- ions in the course of the redox reaction. Moreover, the mesoporous characteristic of GNP determined the time constant of the device, because it can accommodate larger ions even though their transport within the pores may be more difficult.

This observation also demonstrates that in addition to the diffusion of charged species within the porous matrix of the carbons, mass transfer of the redox species is also important when the time

constant of the cells are considered. However, the dissipative property of the cell with LiBr was higher because its C'' value of ca. 0.41 F was larger than that with $MgBr_2$ whose C'' value was 0.27 F [19, 44].

It is well known that in addition to the use of DRS as inherent redox electrolytes, it is also possible to utilise these bromides as additives to inert electrolytes. Furthermore, Na_2SO_4 [45] and $MgSO_4$ [46] have been shown to be viable aqueous electrolytes for supercapacitors, both due to their advantageously wide CPR [6], and also due to the general environmental friendliness of these salts[47].

To investigate the role of the cations in the inert electrolytes on the redox activity of the added bromide salt, 0.15 mol/L of KBr was used. GNP electrodes were used in the EEM cells, with either 1.0 mol/L of Na_2SO_4 or 1.0 mol/L $MgSO_4$. The cells without KBr were denoted as: 1M-Na_2SO_4-GNP and 1M-$MgSO_4$-GNP, whilst those with KBr were designated as: 0.15M-KBr-1M-Na_2SO_4-GNP and 0.15M-KBr-1M-$MgSO_4$-GNP respectively.

The CVs of these cells are presented in Fig. 12a from which it can be noticed that the capacitance of 1M-Na_2SO_4-GNP (ca. 17.9 F/g) was about 6.5% greater than that of 1M-$MgSO_4$-GNP (ca. 16.8 F/g). The cells with 0.15 mol/L KBr as redox additive showed an increase in charge capacity, and the capacity of the cell of 0.15M-KBr-1M-Na_2SO_4-GNP was also slightly larger than that of 0.15M-KBr-1M-$MgSO_4$-GNP.

Considering that the charge capacity of these cells was comparatively similar, the utilisation of either salts for the development of commercial cells would thus be dependent on the availability and safety of the reagents. Since both supporting electrolytes i.e. Na_2SO_4 and $MgSO_4$ are classified as non-hazardous substances[47], commercial applications of any of these reagents should be highly feasible.

In these cells, a special attention was paid to the ion dynamics due to the findings of the roles of cations which have already been described in previous sections. Accordingly, the time constants of these devices which give important information on the contribution to charge storage from the interacting ions within the porous matrix of the electrodes in the cells were studied.

According to Fig. 12b, the time constant of 1M-Na_2SO_4-GNP was ca. 2.5 times smaller than that of 1M-$MgSO_4$-GNP. This can be explained from the standpoint of the ionic properties of the $MgSO_4$ and Na_2SO_4 electrolytes within the porous matrix of the carbon, and more importantly the polarisation power or charge density of Mg^{2+} is greater than that of Na^+. This may result in Mg^{2+} being more likely associated with SO_4^{2-}, and hence less mobile than Na^+ [48, 49].

Interestingly, with the KBr incorporated as DRS into these inert electrolytes, it was observed that the time constants of the resulting devices became identical. That is the time constant of the Na_2SO_4 cell without DRS (i.e. 1M-Na_2SO_4-GNP) which was 15.85 s increased to 19.95 s upon the addition of KBr. This indicates a slight reduction of the capacitive response on the addition of the DRS. Contrastingly, the time constant of the cell with inert $MgSO_4$, i.e. 1M-$MgSO_4$-GNP which was 39.89 s decreased to 19.95 s in the cell 0.15M-KBr-1M-$MgSO_4$-GNP. This means that the use of KBr actually improved the capacitive response of the cell using the $MgSO_4$ electrolyte, but has a slightly reverse effect for the cell with Na_2SO_4.

This finding could probably be due to a change in the charge interaction and activity of the electrolytes containing the hydrated K^+, Mg^{2+} and Br^- ions within the pores of the carbon. For example, it is generally known that the $MgSO_4$ electrolyte could form different cation-anion pairs [50], thus, when dissolved Br^- interacts with this complex, a dual cation-anion pair which could adjust the polarization

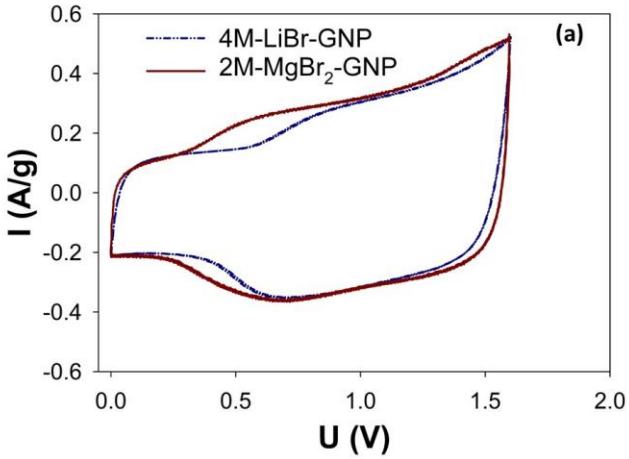

1

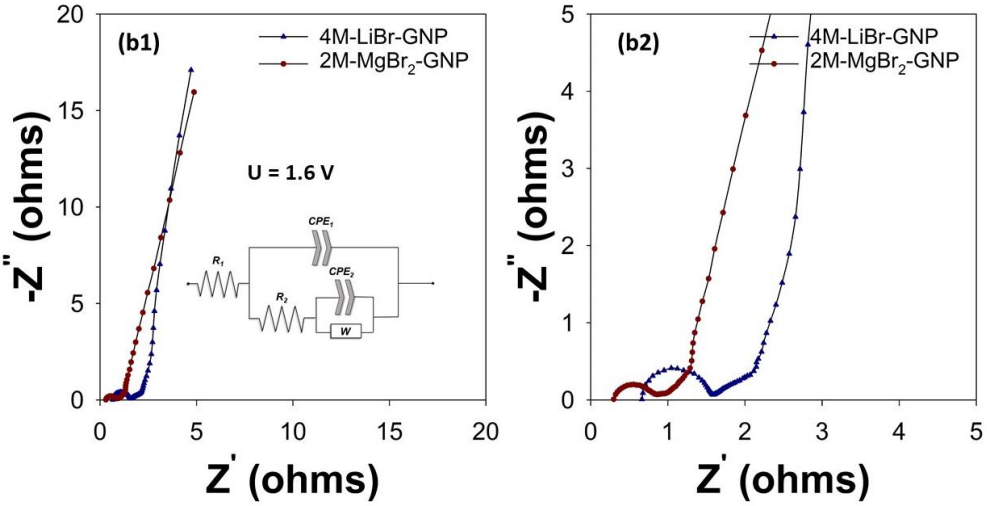

2

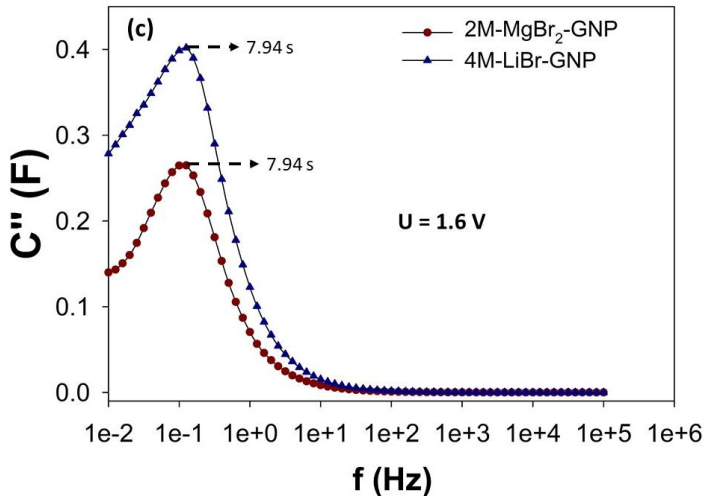

3

4 Figure 11: Performance comparison of 4M-LiBr-GNP with 2M-MgBr$_2$-GNP. (a) CVs with U_L = 1.6 V

5 and scan rate = 10 mV/s. (b) Nyquist plots taken at U_L = 1.6 V. (c) Corresponding Bode plots to (b).

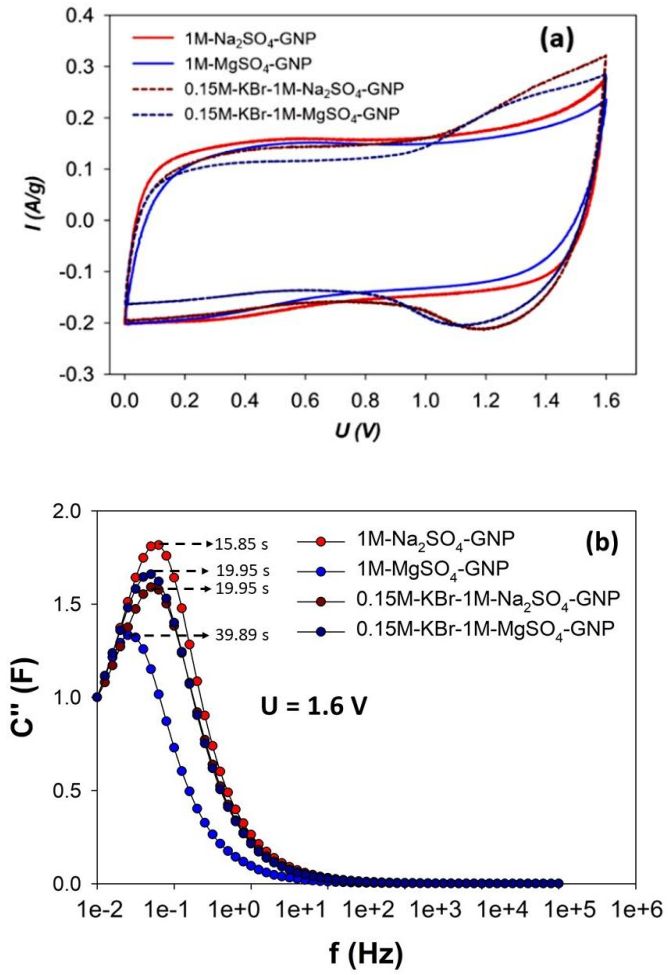

Figure 12: Comparisons between EEM cells fabricated with GNP and using the inert electrolytes 1.0 mol/L $MgSO_4$ or Na_2SO_4 with or without 0.15 mol/L KBr as additive. (a) CVs at U_L = 1.6 V, scan rate: 10 mV/s. (b) C'' *vs* f (Bode plot) at U_L = 1.6 V.

of Mg^{2+} relative to Br^- could be formed. This possible complex ion pairing mechanism may have contributed to reducing the time constant observed in the device with $MgSO_4$ and KBr. Although various experimental studies and molecular dynamics simulation data on cation-anion interactions are available[49], what is of importance to this study and further work is the role played by the cation-anion and ion-solvent interactions within the porous structures of carbons.

Furthermore, the properties of the GNP electrode, particularly its larger pores which can accommodate larger hydrated ions or shared hydration shells, imply that such cation-anion pairs and complexes could also be formed within the confines of the porous matrix.

Thus, since the charge capacity of both 0.15M-KBr-1M-Na_2SO_4-GNP and 0.15M-KBr-1M-$MgSO_4$-GNP are very similar, it means that in the selection of supporting electrolyte the role of possible cation-anion interactions should be considered. Accordingly, this finding might be extended to other combination of additives to critically understand other performance metrics in addition to charge capacity that are actually improved when DRS are used in supercapatteries.

4. Conclusions

The properties of aqueous halide supercapatteries fabricated with two different commercial carbons have been rigorously characterised. The surface properties of the micoroporous activated carbon (AC-2) and the mesoporous highly graphitised carbon, graphene nanoplatelets (GNP) have been analysed. Both carbons contained significant surface oxygen groups, but AC-2 had a comparatively lower C/O ratio. Electrochemical analysis in an inert electrolyte revealed that the EDL capacitance of AC-2 was slightly larger than that of GNP. However, in a redox electrolyte, GNP displayed a markedly enhanced charge capacity compared to AC-2. The improved charge capacity of GNP has been attributed to its mesopores being capable of accommodating more products from the redox reaction, and also to a possible higher surface reactivity enhanced by the morphology of the material.

Generally, whilst the performance metrics of EEM cells with AC-2 as electrodes showed very little sensitivity to change in concentration from 2.0 to 4.0 mol/L LiBr, cells with GNP electrodes displayed a marked improvement in performance with increase in concentration. In line with these observations, the mesoporous property of GNP coupled with the polarisation power and hydration properties of Li^+

have been correlated to the observed features of the supercapattery with GNP as electrodes. This use of a highly graphitised and mesoporous carbon in the design of a relatively high voltage supercapattery is thus important in contrasting to the performance of the common micoroporous carbon which displays comparatively low "active volume storage". Hence, these performance metrics could act as a benchmark for the selection of electrodes in practice.

From a device design standpoint, the effects of KBr as a redox additive to inert electrolytes of Na_2SO_4 or $MgSO_4$ with GNP as electrodes have been studied. Herein, it was shown that on the incorporation of the DRS, the time constant of the device was slightly increased for the former, and decreased for the latter. This observation may be linked to the role of the cation-anion pairs and ion-solvent interaction and their effects within the porous matrix of the carbon. Since a trend expected from the early deployment of DRS in commercial cells may be using the DRS as additives, findings from this work should contribute to the understanding of the interplay between the solvation properties of the non-active counter-ions relative to the performance of the device.

Acknowledgement

This work received funding from the International Doctoral Innovation Centre, Ningbo Education Bureau, Ningbo Science and Technology Bureau, and the University of Nottingham, and Ningbo Municipal Government (3315 Plan and 2014A35001-1).

Bamidele Akinwolemiwa, ORCID: https://orcid.org/0000-0001-6389-3908

Chaowei Wei, ORCID**:** https://orcid.org/0000-0002-1869-443X

George Zheng Chen, ORCID: https://orcid.org/0000-0002-5589-5767

References

1. T. Lin, I.-W. Chen, F. Liu, C. Yang, H. Bi, F. Xu and F. Huang, *Science*, 2015, **350**, 1508-1513.
2. L. Suo, O. Borodin, T. Gao, M. Olguin, J. Ho, X. Fan, C. Luo, C. Wang and K. Xu, *Science*, 2015, **350**, 938-943.
3. J. Sun, C. Wu, X. Sun, H. Hu, C. Zhi, L. Hou and C. J. J. o. M. C. A. Yuan, 2017, **5**, 9443-9464.
4. C. Peng, S. Zhang, X. Zhou and G. Z. Chen, *Energy & Environmental Science*, 2010, **3**, 1499-1502.
5. S. Makino, Y. Shinohara, T. Ban, W. Shimizu, K. Takahashi, N. Imanishi and W. Sugimoto, *RSC Advances*, 2012, **2**, 12144-12147.
6. K. Fic, M. Meller, J. Menzel and E. Frackowiak, *Electrochimica Acta*, 2016, **206**, 496-503.
7. B. Akinwolemiwa, C. Peng and G. Z. Chen, *Journal of The Electrochemical Society*, 2015, **162**, A5054-A5059.
8. S.-E. Chun, B. Evanko, X. Wang, D. Vonlanthen, X. Ji, G. D. Stucky and S. W. Boettcher, *Nature communications*, 2015, **6**.
9. B. Akinwolemiwa, C. Wei, Q. Yang, L. Yu, L. Xia, D. Hu, C. Peng and G. Z. Chen, *Journal of The Electrochemical Society*, 2018, **165**, A4067-A4076.
10. S. T. Senthilkumar, R. K. Selvan and J. S. Melo, *Journal of Materials Chemistry A*, 2013, **1**, 12386-12394.
11. S. J. Yoo, B. Evanko, X. Wang, M. Romelczyk, A. Taylor, X. Ji, S. W. Boettcher and G. D. Stucky, *Journal of the American Chemical Society*, 2017, **137**, 9985-9993.
12. M. Xia, J. Nie, Z. Zhang, X. Lu and Z. L. J. N. E. Wang, 2018, **47**, 43-50.
13. P. Díaz, Z. González, R. Santamaría, M. Granda, R. Menéndez and C. Blanco, *Electrochimica Acta*, 2015, **168**, 277-284.
14. E. Frackowiak, K. Fic, M. Meller and G. Lota, *ChemSusChem*, 2012, **5**, 1181-1185.
15. L.-Q. Mai, A. Minhas-Khan, X. Tian, K. M. Hercule, Y.-L. Zhao, X. Lin and X. Xu, *Nature communications*, 2013, **4**.

16. M. D. Stoller and R. S. Ruoff, *Energy & Environmental Science*, 2010, **3**, 1294-1301.
17. K. M. Košiček, K. Kvastek and V. J. E. A. Horvat-Radošević, 2016, **195**, 77-84.
18. C. Jing, X. Song, K. Li, Y. Zhang, X. Liu, B. Dong, F. Dong, S. Zhao, H. Yao and Y. J. J. o. M. C. A. Zhang, 2020, **8**, 1697-1708.
19. P. Taberna, P. Simon and J.-F. Fauvarque, *Journal of The Electrochemical Society*, 2003, **150**, A292-A300.
20. S. Porada, R. Zhao, A. Van Der Wal, V. Presser and P. Biesheuvel, *Progress in Materials Science*, 2013, **58**, 1388-1442.
21. J. Gamby, P. Taberna, P. Simon, J. Fauvarque and M. Chesneau, *Journal of power sources*, 2001, **101**, 109-116.
22. K. A. Cychosz and M. Thommes, *Engineering*, 2018.
23. K. A. Cychosz, X. Guo, W. Fan, R. Cimino, G. Y. Gor, M. Tsapatsis, A. V. Neimark and M. Thommes, *Langmuir*, 2012, **28**, 12647-12654.
24. M. Thommes, K. Kaneko, A. V. Neimark, J. P. Olivier, F. Rodriguez-Reinoso, J. Rouquerol and K. S. Sing, *Pure and Applied Chemistry*, 2015, **87**, 1051-1069.
25. J. Li, J. O'Shea, X. Hou and G. Z. Chen, *Chemical Communications*, 2017, **53**, 10414-10417.
26. C. Wei, B. Akinwolemiwa, L. Yu, D. Hu and G. Z. Chen, in *Polymer Composites with Functionalized Nanoparticles*, eds. K. Pielichowski and T. M. Majka, Elsevier, 2019, DOI: https://doi.org/10.1016/B978-0-12-814064-2.00007-X, pp. 211-248.
27. Y. Munaiah, P. Ragupathy and V. K. Pillai, *Journal of The Electrochemical Society*, 2016, **163**, A2899-A2910.
28. J. R. Gaier, N. F. Ditmars and A. R. Dillon, *Carbon*, 2005, **43**, 189-193.
29. J. Xu, I. Y. Jeon, J. M. Seo, S. Dou, L. Dai and J. B. Baek, *Advanced materials*, 2014, **26**, 7317-7323.

30. E. D. Grayfer, V. G. Makotchenko, A. S. Nazarov, S.-J. Kim and V. E. Fedorov, *Russian Chemical Reviews*, 2011, **80**, 751-770.
31. H. Zhou, H. Zhang, P. Zhao and B. Yi, *Electrochimica Acta*, 2006, **51**, 6304-6312.
32. B. E. Conway, *Electrochemical Supercapacitors: Scientific fundamentals and technological applications*, Kluwer-Plenum, New York, 1999.
33. W. G. Pell and B. E. Conway, *Journal of Power Sources*, 2004, **136**, 334-345.
34. D. M. Ford and E. D. Glandt, *Journal of membrane science*, 1995, **107**, 47-57.
35. M. Meller, J. Menzel, K. Fic, D. Gastol and E. Frackowiak, *Solid State Ionics*, 2014, **265**, 61-67.
36. W. Eeles and J. Turnbull, *Proc. R. Soc. Lond. A*, 1965, **283**, 179-193.
37. B. R. Puri and R. Bansal, *Carbon*, 1966, **3**, 533-539.
38. L. Gordeeva, G. Restuccia, A. Freni and Y. I. Aristov, *Fuel processing technology*, 2002, **79**, 225-231.
39. A. Burke and M. Miller, *Electrochimica Acta*, 2010, **55**, 7538-7548.
40. J. R. Gaier, *Synthetic metals*, 1987, **22**, 15-22.
41. L. Demarconnay, E. Raymundo-Pinero and F. Béguin, *Journal of Power Sources*, 2011, **196**, 580-586.
42. S. Kondrat, C. Perez, V. Presser, Y. Gogotsi and A. Kornyshev, *Energy & Environmental Science*, 2012, **5**, 6474-6479.
43. J. Segalini, E. Iwama, P.-L. Taberna, Y. Gogotsi and P. Simon, *Electrochemistry Communications*, 2012, **15**, 63-65.
44. M. E. Orazem and B. Tribollet, *Electrochemical impedance spectroscopy*, John Wiley & Sons, 2011.
45. L. Demarconnay, E. Raymundo-Piñero and F. Béguin, *Electrochemistry Communications*, 2010, **12**, 1275-1278.

46. J. Menzel, K. Fic and E. Frackowiak, *Progress in Natural Science: Materials International*, 2015, **25**, 642-649.
47. SIGMA-ALDRICH, Chemical Safety Data Sheet, https://www.sigmaaldrich.com/united-kingdom.html, (accessed 5th January, 2018).
48. P. J. Lenart, A. Jusufi and A. Z. Panagiotopoulos, *The Journal of chemical physics*, 2007, **126**, 044509.
49. J. Barthel, H. Hetzenauer and R. Buchner, *Berichte der Bunsengesellschaft für physikalische Chemie*, 1992, **96**, 988-997.
50. R. Buchner, T. Chen and G. Hefter, *The Journal of Physical Chemistry B*, 2004, **108**, 2365-2375.